Ballistic behavior of high hardness perforated armor plates against 7.62 mm armor piercing projectile

Namık Kılıç [a,*], Said Bedir [a], Atıl Erdik [a], Bülent Ekici [b], Alper Taşdemirci [c], Mustafa Güden [c]

[a] Computer Aided Engineering Department, Otokar Otomotiv ve Savunma San. A.S, Atatürk Cad No: 9, Arifiye, 54580 Sakarya, Turkiye
[b] Department of Mechanical Engineering, Faculty of Engineering, Marmara University, 34722 Istanbul, Turkiye
[c] Department of Mechanical Engineering, Faculty of Engineering, Izmir Institute of Technology, 35430 Gülbahçe Izmir, Turkiye

ABSTRACT

In this paper, some of the important defeating mechanisms of the high hardness perforated plates against 7.62 × 54 armor piercing ammunition were investigated. The experimental and numerical results identified three defeating mechanisms effective on perforated armor plates which are the asymmetric forces deviates the bullet from its incident trajectory, the bullet core fracture and the bullet core nose erosion. The initial tests were performed on the monolithic armor plates of 9 and 20 mm thickness to verify the fidelity of the simulation and material model parameters. The stochastic nature of the ballistic tests on perforated armor plates was analyzed based on the bullet impact zone with respect to holes. Various scenarios including without and with bullet failure models were further investigated to determine the mechanisms of the bullet failure. The agreement between numerical and experimental results had significantly increased with including the bullet failure criterion and the bullet nose erosion threshold into the simulation. As shown in results, good agreement between Ls-Dyna simulations and experimental data was achieved and the defeating mechanism of perforated plates was clearly demonstrated.

© 2014 Elsevier Ltd. All rights reserved.

1. Introduction

High strength steel perforated plates are industrially available for many years in armor systems to improve ballistic performance by introducing various shaped configurations. In perforated plate armor, usually the holes or slits are designed to interact with the diameter of the threat and performance of such armor solution is determined by strength of the material, thickness of plate and orientation of holes. The shape of each hole can be same or different, and can be in the form of slits and their arrangement can be regular or irregular [1]. Theoretically, when bullet impacts side of a hole on perforated plate armor, bending stress is generated to break incoming projectile core or at least projectile is diverted from its incident trajectory and thus reduce its penetration capability.

The perforated plate armor, which was first suggested by Ben-Moshe [2] in 1986, was based on evenly drilled holes on a high hardness steel plate. The diameter of the holes and their spacing were designed to defeat the small arm ammunitions in the range of 5.56–14.5 calibers. Auyer et al. [3] invented a ballistic protection package consisted of triangular shaped perforations on heat treated steel plates. Hole's patterns of the outer and inner perforated plates were offset with respect to each other to prevent straight line penetration of projectile. Ravid and Hirchberg [4] proposed a ballistic solution package with an auxiliary high hardness steel perforated plate that the total area of holes was about between 40–50%. The holes of the auxiliary perforated plate were disposed with center to center spacing from 1.2 to 1.9 times the diameter of hole to defeat small arm threats. In Norris and Smith [5] invention, armor plate had slot shaped perforation in which slots were angled with respect to sides of the plate. This class of appliqué armor is also known as P900 and used by US army ground combat systems against small-arm threats. The use of perforated plates as add-on armor increases the mass efficiency; for example the increase was reported as much as 2.4 when impacted with 7.62 mm AP ammunition [6].

Although the idea of using geometric perforation to increase ballistic protection was suggested in some patents, the number of experimental and numerical studies on this topic is significantly less. In a recent work, Balos et al. [7] shown mass effectiveness of the perforated plates against 12.7 mm M-8 API threat by investigating the effect of geometry, mechanical properties, thickness, obliquity and gap. In the subsequent experimental study conducted by Radisavljevic et al. [8] an attempt was made to design an affective perforated plate solution by investigating hole size and ligament length between holes. Mishra et al. [9,10] found

---

experimentally that the performance of an armor plate can be dramatically enhanced by drilling regular pattern of holes on it. Howell et al. [11] studied high manganese and high aluminum austenitic steels for application of P900 perforated armor according to MIL-PRF-32269. With ballistic tests, areal density equivalence against 7.62 caliber armor piercing projectile was found.

The first numerical study authors are aware of was carried out by Chocron et al. [12]. In this study, impact of 7.62 mm AP ammunition against edge of a metallic target was investigated to explain the defeating mechanism. The induced bending stress and resulting strain was calculated to demonstrate projectile fracture experienced in shot tests. In another study, Rosenberg et al. [13] attempted to demonstrate significant mechanisms for defeating AP projectiles. With ballistic experiments and 3D numerical simulations, it was shown that an inclined plate of high strength steel can induce shattering to an AP projectile.

High velocity impact and penetration problems include large deformation, erosion, high strain rate dependent nonlinear material behavior and fragmentation. Therefore, it is important to model the penetration where above effects are taken into account. Numerical methods and corresponding computing technologies have been evolved to the level where complex deformation and penetration pattern during ballistic impact can be accurately predicted. A review of the open literature on impact simulations shows that the most research in this field have been focused on the development and application of continuum hydro-codes [14–17]. A popular explicit code, Ls-Dyna was successfully used to simulate several types of armors subjected to impact for various threat levels and capable of applying various simulation approaches [18–23]. Borvik et al. [18] studied the behavior of Weldox 460 E steel plates impacted by blunt nosed cylindrical projectiles. In order to describe penetration behavior, they developed a material characterization test program to find out Johnson–Cook (J–C) strength and failure models for Weldox 460 E steel. The projectile used in 2D numerical simulation was modeled as linear elastic with Young's modulus of 200 GPa and Poisson's ratio of 0.33 due to lack of reliable material data. The plug formation was successfully simulated. Buchar et al. [19] presented ballistic performance of dual harness steel armor against 7.62 mm armor piercing projectile and found significant agreement between tests and numerical results. One of the important feature of this study is the J–C strength parameters of hardened steel projectile was given. Borvik et al. [20] modeled projectile with elastic–plastic strain rate independent material with isotropic hardening and investigated shape effect of projectile with simulations performed on Ls-Dyna. With adaptive meshing approach numerical issues were eliminated and reasonable agreement was achieved to find ballistic limit velocity. Teng et al. [21] evaluated ballistic performance of double layered steels against projectiles impacted at sub-ordnance velocities and found that by layering, ballistic limit can be improved up to 25%. Dey et al. [22] have studied ballistic perforation resistance of monolithic and layered 12 mm Weldox 700 steel targets with gas gun fired ogival projectiles which have 52 HRc hardness. Comprehensive strength and failure models were given for armor plate but hardened steel projectile was modeled as an elastic–plastic material with bilinear isotropic hardening without fracture. One of the significant articles on ballistic simulation has been presented by Borvik et al. [23]. They considered ballistic penetration performance of five different high hardness steel alloys. Based on test results, almost a linear correlation between ballistic limit velocity and yield strength was found. All these studies show that the ballistic performance of monolithic and layered steel targets can be predicted with well developed finite element numerical models.

The numerical simulations of the ballistic testing of perforated plates require complex capability in 3D. The fidelity of the simulations has strong dependency on the material strength and failure models for both target and bullet. In the first part of the study, the impact tests were performed on the monolithic plates to validate the fidelity of the material model parameters. Then, the layered armor was subjected to the ballistic tests and the tests were simulated. The stochastic nature of the ballistic tests on the perforated plate was analyzed based on the bullet impact zone with respect to holes. Various cases including without and with bullet failure models were further investigated to identify the mechanisms of bullet failure. The results of present study provided further insights on the defeating mechanisms of perforated armors.

2. Materials and testing

The steel used in the present study is Secure 500 which is an alloyed, liquid-quenched and tempered high strength special steel. The mechanical properties of the alloy specified by the manufacturer are tabulated in Table 1. The alloy has the minimum yield and tensile strength of 1300 and 1600 MPa, respectively. The dimensions of the ballistic test plates including monolithic and perforated armor plates were in 400×400 mm^2, which was in according NATO Stanag 4569 standard [24]. The dimensions of the plates ensured that the stress waves reflected from the edge induced no forces on the bullet during the course of the penetration. The target plates were mounted on a stiff frame in the ballistic test set-up and each target was subjected to four shoots.

Ballistic tests on monolithic armor plates were carried out to investigate penetration behavior for two different thicknesses. In 20 mm case, the bullet was captured by target plate and in 9 mm case passed through. The geometric model of the layered armor is shown in Fig. 1a. The perforated and base armor plates are sequentially 6 mm and 9 mm in thickness, and placed with a gap of 30 mm. The plates were fixed to each other using four spacers inserted at the corners. The 6 mm diameter hole perforations were formed by laser cutting. The distance between the centers of holes was 10 mm. The size and geometrical arrangement of the holes were not subjected to a systematic optimization study; but, the general aspects of design available in the commercial applications were applied, for example the diameter of holes was smaller than the ammunition diameter (7.8 mm). The ballistic tests were performed using NATO Stanag 4569 standard [24]. Stanag 4569 specifies the protection levels for logistic and armored vehicles in five classes. The threat subject to this study is denoted by Level-3, in which the ammunition is named as 7.62×54 B32 API and impact velocity is 854 m/s with a tolerance of +/20 m/s. The armor piercing bullet is composed of brass jacket, hardened steel core, sabot, lead-antimony cap and point fillers as shown in Fig. 1b. The total mass of the bullet was about 10 g. The measured outer diameter, the core diameter and the core length of the bullet were sequentially 7.8 mm, 6.2 mm and 28.2 mm as depicted in Fig. 1c. The bullet was in ogival shape with a radius of 15 mm and with an ogive angle of ~30°. The hardness near the tip of the core was measured as 880 Vickers Hardness. A rough estimation of the ultimate tensile strength of the core using the hardness number (3 × Vickers Hardness)) gives a value of 2500 MPa. The picture and the schematic representation of ballistic test facility are shown in Fig. 2. The velocity of the bullet was adjusted by the amount of powder in the cartridge and kept around 854 m s^{-1} as stated in Stanag 4569. The velocity of the bullet was measured by means of a

Table 1
The mechanical properties of Secure 500 armor steel.

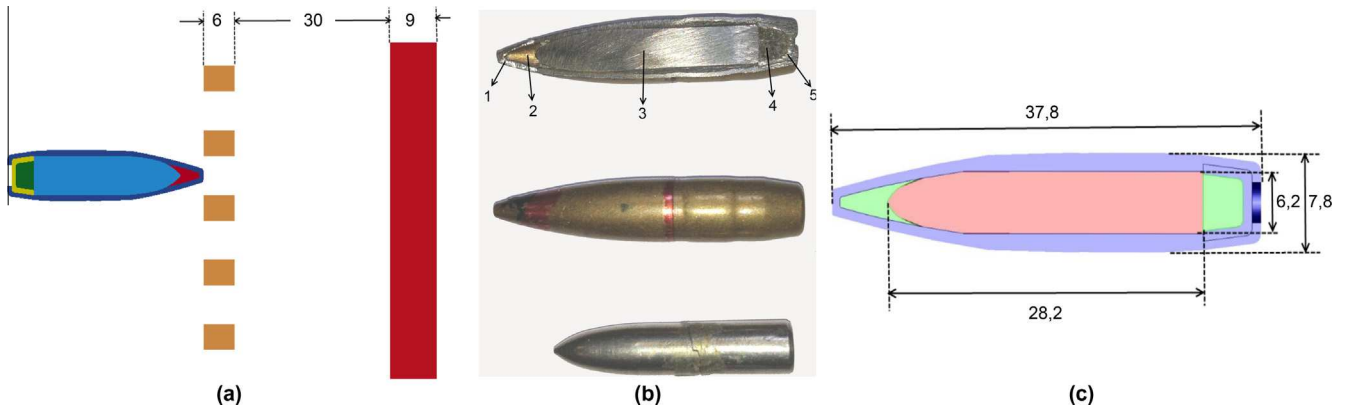| Hardness (Vickers)	Tensile strength (MPa)	Yield strength (MPa)	Elongation at break (%)
480–530	1600	1300	9

Fig. 1. (a) The model of the layered (perforated and unperforated base) armor test plates; the cross-section view of 6 mm perforated plate, 30 mm gap and 9 mm thick unperforated base plate, (b) 7.62 mm AP bullet and the parts: 1 – brass jacket, 2 – point filler, 3 – hardened steel core, 4 – lead base filler and 5 – sabot and (c) the bullet assembly dimensions in mm.
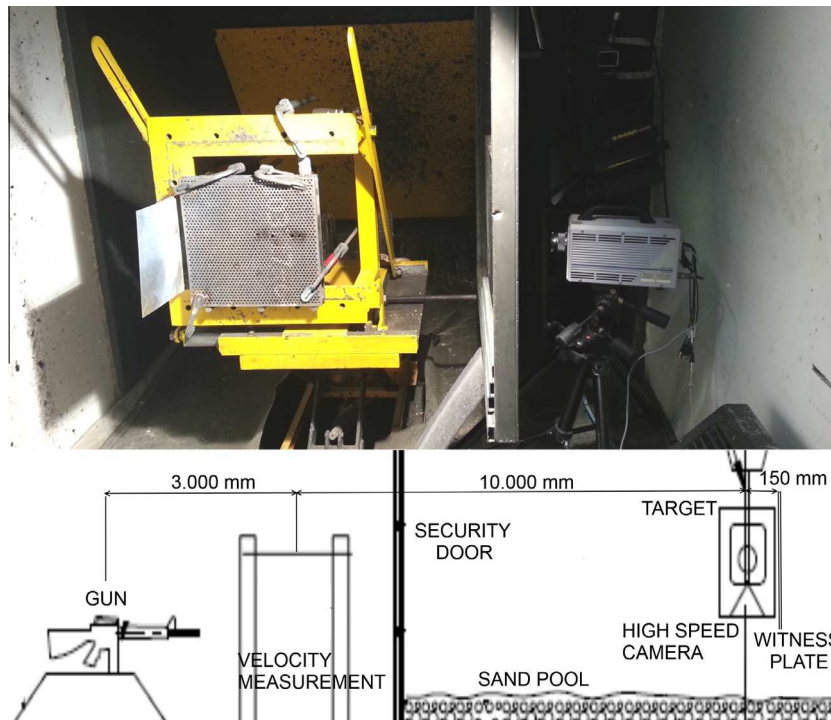

Fig. 2. The ballistic test set-up: the pictures of the target and high speed camera and the schematic of the velocity measurement system.

precise chronometer synchronized with two led photovoltaic detectors inserted 2 m apart. The velocity measurement system was placed 10 m away from the target. An aluminum witness plate was placed 150 mm away from target and the fragmentation and spall behavior of target and the residual velocity of the bullet were determined using a high speed camera (46 000 fps with 256 × 176 pixel resolution).

The Johnson–Cook (J–C) flow stress model is one of the most widely used material models of the ballistic penetration studies and available in the commercial hydro-codes [25]. It is a visco-plastic material model, particularly developed for the ductile metals. The model includes the strain hardening, strain rate hardening and thermal softening effects on the material flow stress. The equivalent stress (σ_y) in the flow stress model is expressed as,

$$\sigma_y = [A + B\varepsilon_p^n][1 + C \ln\dot{\varepsilon}_p^*][1 - T_H^m] \tag{1}$$

where ε_p is the equivalent plastic strain, $\dot{\varepsilon}_p^*$ is the strain rate ratio, given as $\frac{\dot{\varepsilon}_p}{\dot{\varepsilon}_o}$, where $\dot{\varepsilon}_p$ is the equivalent plastic strain rate, $\dot{\varepsilon}_o$ is the reference equivalent plastic strain rate, and T_H is the normalized temperature, expressed as $T = \frac{T - T_r}{T_m - T_r}$; where T, T_r and T_m are the temperature, room temperature and melting temperature, respectively. There are five material constants to be determined in the J–C flow stress model: A, B, n, C, and m. The first bracket in Eq. (1) gives the stress as a function of plastic strain at the reference strain rate and room temperature. The expressions in the second and third brackets represent the effect of strain rate and thermal softening, respectively.

The J–C damage model includes the effects of stress triaxiality, temperature and strain rate on the failure strain [26]. The J–C damage model is a cumulative damage-fracture model which takes into account the loading history. The model assumes that the damage accumulates in the material during plastic straining and the frac-

ture occurs immediately when the damage reaches a critical value. The damage is defined by a cumulative damage law as:

$$D = \sum \frac{\Delta \varepsilon}{\varepsilon^f} \quad (2)$$

where $\Delta \varepsilon$ is the increment of the plastic strain during an integration cycle and ε^f is the equivalent fracture strain under the current conditions of stress, strain rate and temperature. The damage variable D takes a value between 0 and 1; where $D = 0$ represents undamaged material and $D = 1$ represents failed element. The J–C damage model is expressed as,

$$\varepsilon^f = [D_1 + D_2 \exp(D_3 \sigma^*)][1 + D_4 \; ln\dot{\varepsilon}_p^*][1 + D_5 T_H^m] \quad (3)$$

where σ^* is the stress triaxiality and for a notched round sample it is given as [26],

$$\sigma^* = \frac{\sigma_H}{\sigma_{eq}} = \frac{1}{3} + ln\left(1 + \frac{a}{2R}\right) \quad (4)$$

where, σ_h is the hydrostatic stress, σ_{eq} is the effective or equivalent stress and a and R are sequentially the radius of the smallest cross section and the radius of curvature at the neck. There are five material constants to be determined in the J–C damage model: $D_1, D_2, D_3,$
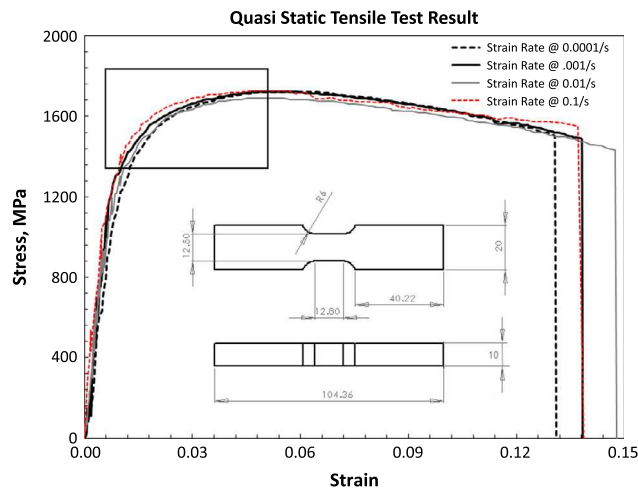
D_4 and D_5. The constants, D_1, D_2 and D_3 are mostly dependent on the stress state and the constants D_4 and D_5 on the strain rate hardening and thermal softening respectively.

The J–C material and damage model parameters of Secure 500 and 7.62 armor piercing bullet core were previously determined [27]. The details of the experimentations, the quasi-static and dynamic testing methods and J–C flow stress and failure model determination can be found in Ref. [28]. Fig. 3 shows the quasi-static stress strain curve of Secure 500. The J–C material model parameters of the hardened steel core of the bullet core (830–880 HV) were determined by tensile testing of non-standard miniature (2 mm in diameter and 10 mm in gage length) dog-bone shape test specimens [27]. The failure parameters of the core could not be determined as it was very difficult to machine the hardened steel core to prepare notched specimens to induce different stress triaxialities.

The material model parameters of the target, bullet and jacket used in the simulations are tabulated in Table 2. The J–C material models of Armox 500T and Secure 500 armor steels are valuable references which have same hardness values to compare with own data. Using the parameters found in literature, the stress–strain curves at 1250 s^{-1} strain rate are visualized in Fig. 4a. Similar comparison is also performed for hardened steel core. Due to the difficulties experienced during specimen preparation a comparative study with the literature based material models would increase confidence level before simulation. The stress–strain curves of Armox 500T alloy derived from the J–C flow stress model parameters reported in Refs. [29,30] and the stress–strain curves of Secure 500 alloy derived from the J–C flow stress model parameters reported in Ref. [31] are shown for comparison. The J–C model stress–strain curve of the bullet core is shown in Fig. 4b at the strain rate of 1250 s^{-1}. For comparison, the stress–strain curves of the core derived from published works in Refs. [16,20,32] are also drawn in the same figure. The core model stress–strain curve shows close agreement with the J–C model in Ref. [16].

The Mie-Gruneisen equation of state (EOS) was used in the simulations. The Mie-Gruneisen EOS is given as [33],

$$P = \frac{\rho_o c^2 \mu (1 + (1 - \frac{\gamma}{2})\mu - (\frac{\alpha}{2})\mu^2)}{\left[1 - (S_1 - 1)\mu - \frac{S_2 \mu^2}{(\mu+1)} - \frac{S_3 \mu^3}{(1+\mu)^2}\right]} + (\gamma + \alpha\mu)E_o \quad (5)$$

where E_0 is the internal energy per unit volume, c is the intercept of the shock and particle velocity curve, S_1, S_2 and S_3 are the coefficients of the slope of the shock and particle velocity curve and γ
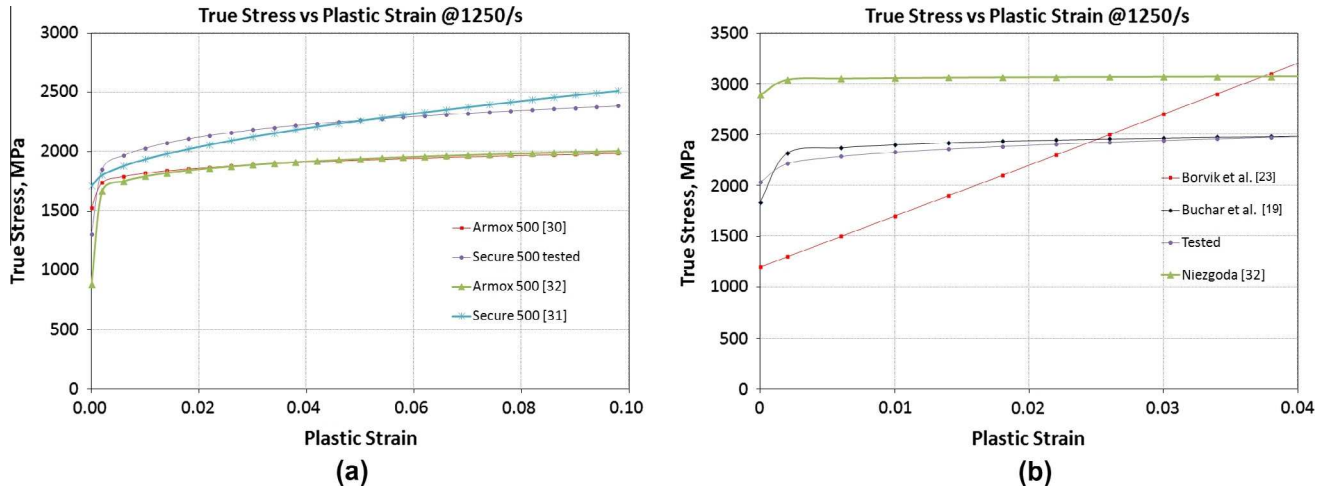

Fig. 3. The experimental quasi-static tensile stress–strain curves of the target plate.

Table 2
The material and J–C model parameters of the target, bullet core and jacket.

Definition	Symbol	Unit	Target material [27]	Bullet core [27]	Cartridge brass [26]
Density	ρ	kg m^{-3}	7850	7850	8960
Elastic modulus	E	GPa	206	206	124
Shear modulus	G	GPa	80	80	46
Poisson's ratio	v	–	0.3	0.3	0.34
Strain hardening	A	MPa	1200	1900	90
	B	MPa	1580	1100	292
	n	–	0.175	0.065	0.31
Strain rate hardening	C	–	0.004	0.05	0.025
Reference strain rate	$\dot{\varepsilon}_0$	s^{-1}	1×10^{-4}	1×10^{-3}	1
Temperature softening	C_p	J kg^{-1} K^{-1}	450	477	386
	T_r	K	300	300	300
	T_m	K	1800	1800	1356
	m	–	1	1	1.09
J–C failure	D_1	–	0.1	No failure criteria defined	0.54
	D_2	–	0.4		4.89
	D_3	–	−1.3		−3.03
	D_4	–	0.05		0.014
	D_5	–	0		1.12
	$\dot{\varepsilon}_0$	s^{-1}	1×10^{-4}		1

Fig. 4. Present and literature J–C flow stress model stress–strain curves at the strain rate of 1250 s^{-1} (a) target plate and (b) bullet core.

Table 3
Equation of state parameters of the target, bullet core and jacket.

Definition	Symbol	Unit	Target material [35]	Bullet core [32]	Cartridge brass [36]
Density	ρ	kg m^{-3}	7850	7850	8960
Elastic wave velocity	C	m s^{-1}	4570	4570	3940
Slope values	S_1	–	1.73	1.49	1.49
	S_2	–	0	0	0
	S_3	–	0	0	0
Gruneisen coefficient	γ	–	1.67	1.93	1.99
Volume correction factor	α	–	–	0.5	0

is the Gruneisen coefficient. The parameter α is the volume correction factor and μ is the compression factor. The Mie Gruneisen EOS parameters of the target, bullet and jacket used in the simulations are tabulated in Table 3.

3. Numerical models

In numerical model, the material is discretised into finite sections over which, the conservation and constitutive equations are solved. The way in which this spatial discretisation is performed leads to different numerical methods. The most commonly used spatial discretizations are Lagrange, Euler, ALE (Arbitrary Lagrange Euler – a mixture of Lagrange and Euler), and meshfree methods such as SPH (Smooth Particles Hydrodynamics). Kilic and Ekici [27] presented a comparative study to demonstrate applicability of Lagrange and SPH techniques on determination of ballistic performance and concluded that, Lagrange method is more effective in visualizing target deformation pattern with respect to SPH. In the Lagrange method the numerical grid moves and deforms with the material, which is ideal for following the material motion and deformation in regions of relatively low distortion, and possibly large displacement. This formulation is widely used because its advantages, such as being able to track accurately and efficiently material interfaces and incorporate complex material models. Conservation of mass is automatically satisfied and material boundaries are clearly defined. The disadvantage of Lagrange is that the numerical grid can become severely distorted or tangled in an extremely deformed region, which can lead to adverse effects on the integration time step and accuracy. Very well known negative volume error occurs as a result of this mesh tangling. However, these problems can be overcome to a certain extent by applying numerical techniques such as adaptive meshing, erosion and rezoning [20].

In this study, the mesh model is prepared using the commercial code Hypermesh and numerical simulations were performed using LS-Dyna. The geometric model of monolithic plates was composed of 300 mm diameter circular armor steel plate and bullet as shown in Fig. 5a. A small radius was introduced to the tip of the hardened steel core to allow the smooth mesh transition. The plate was meshed with hexagonal eight node solid elements in three different zones; bullet contact, middle and outer zones (Fig. 5a). The mesh size increases in radial direction from the bullet contact zone to outer zone and varies between 0.2 and 1 mm in size. The mesh transition between the regions prevented the stress wave reflections at the boundaries. The bullet core, jacket, front and rear filler and sabot were meshed with 0.2 mm hexagonal elements. The lead-antimony caps are modeled with material card ISOTROPIC-ELASTIC-FAILURE. ERODING_NODES_TO_SURFACE and EROD-ING_SINGLE_SURFACE contact algorithms were used to simulate the contact between surfaces during penetration. Erosion option, dynamic and static friction and bucket sort frequency were chosen to achieve penetration depths close to found in the ballistic experiments. Time step scale factor was used to establish numerical stability. To eliminate zero energy deformation, hourglass parameters were used to control the simulation. As similar with monolithic plate, the perforated plate was meshed with varying sizes (0.25–1 mm) in three regions as shown in Fig. 5b. The base plate was modeled with mesh sizes of 0.5 mm in the contact, 0.7 mm in the middle and 1.5 mm in the outer zone. The bullet was modeled with the same model parameters used in the monolithic plate model.

4. Results and discussion

The pictures of the front face and the cross-section of 20 mm thickness monolithic plate after the ballistic test are shown in
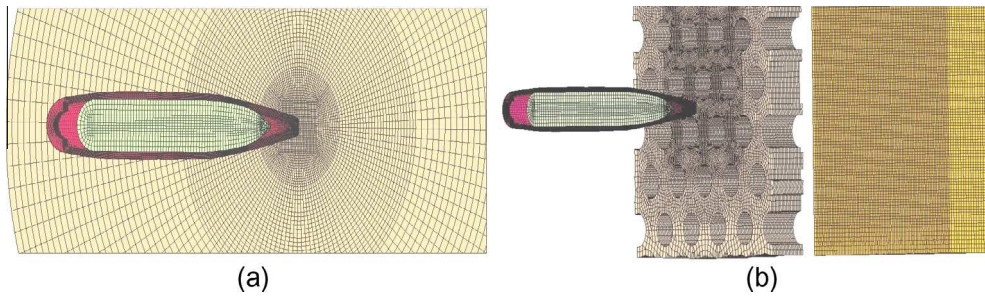
Fig. 5. FE mesh model of (a) unperforated and (b) layered armor plates.
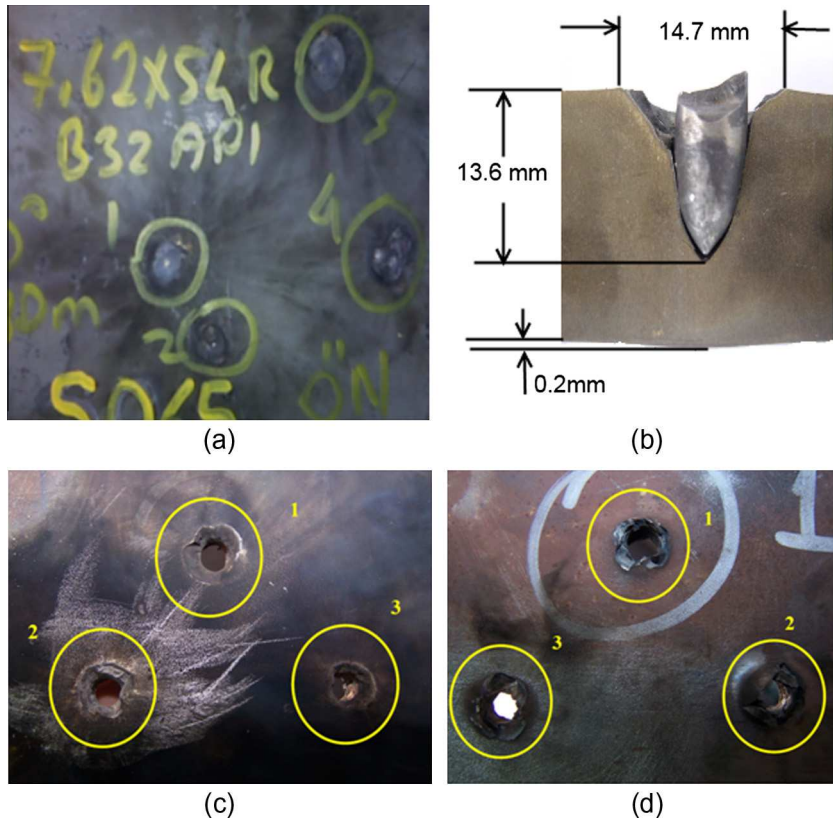

Fig. 6. The pictures of monolithic plate after the test (a) 20 mm thick target front face, (b) 20 mm thick target cross-section, (c) 9 mm thick target front face and (d) 9 mm thick target rear face.

Fig. 6a and b, respectively. As seen in Fig. 6b, the bullet partially penetrated the plate and was captured. The depth of the bullet penetration in tests was varied between 12.5 and 13.6 mm and the average depth of penetration after four shots was calculated as 12.9 mm. The bullet velocity *vs.* time graph of 20 mm thick monolithic plate is shown in Fig. 7 together with the simulation pictures of the bullet and plate at various times. As shown in Fig. 7, the bullet initial velocity, 854 m s^{-1}, gradually declines as it penetrates the target and come to rest after about 0.035 ms. The jacket indents the target at $t = 0.006$ ms; thereafter, lead-antimony insert starts to erode. The damage on the plate develops in the contact zone and when the damage reaches a critical value in an element, the element erodes with no remaining strength. The penetration depth found numerically is nearly the same when compared with experimental results (penetration depth found in simulation is 12.9 mm). Although the ductile cavity formation behavior is successively simulated in the numerical model as shown in Fig. 7, the crater diameter deviates by 20% from the
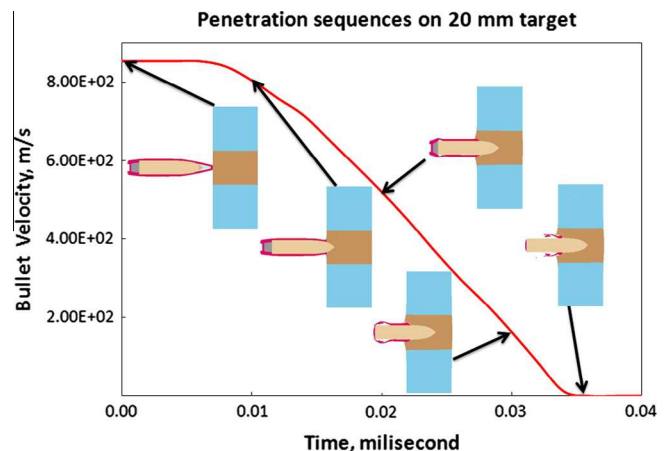

Fig. 7. Numerical bullet velocity *vs.* time graph of 20 mm thick target and the numerical pictures of the bullet and plate at various times.
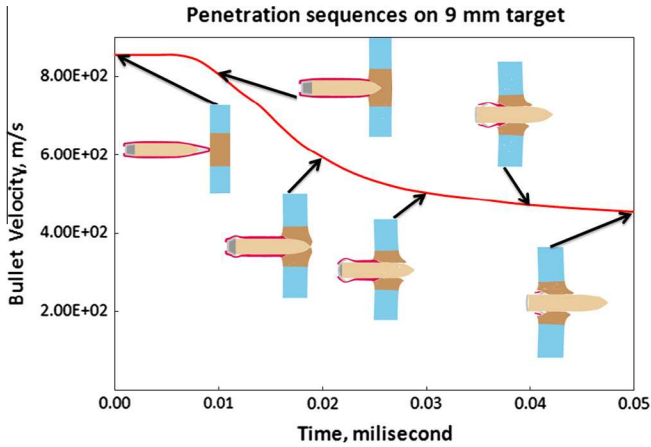
Fig. 8. Numerical bullet velocity *vs.* time graph of 9 mm thick target and the numerical pictures of the bullet and plate at various times.

experimental crater diameter (experimental results varies between 13.1 and 15.5 mm and numerical value is 9.9 mm). It is also noted that the front face spall formation observed in the experiments are not observed in the simulations. The bulge formation is well captured by the numerical model. The bullet fractured into two pieces, which was mainly driven by the shear forces developed on the bullet.

The pictures of the front and rear surface of 9 mm thickness target after the ballistic test are shown in Fig. 6c and d. The residual velocity of the bullet varied between 460 and 495 m s^{-1} with an average of 487 m s^{-1}. The spall formation at the front face after the first and second tests can be clearly seen in Fig. 6c. Both, petal and spall formation are seen at the rear faces (Fig. 6d). As similar with 20 mm thick plate, the tip of hardened steel core in 9 mm thick plate did not deformed and the steel core was fractured into

two or more pieces after the test. The bullet velocity *vs.* time graph of 9 mm thickness monolithic plate is shown in Fig. 8. The numerical residual velocity of the bullet (455 m s^{-1}) is slightly lower than that of the experiments (487 m s^{-1}). From the simulations, the numerical model seems to capture the perforation behavior during the penetration and promising results are obtained to use model parameters in perforated plate simulations.

The ballistic limit thickness of Secure 500 armor steel against 7.62 × 54 API ammunition was previously determined as 15 mm [27]. In order to show mass effectiveness, total thickness of the layered target assembly was kept the same, 15 mm (6 mm thickness perforated plate and 9 mm thickness base plate). The mass areal density of the armor plate was decreased from 117 to 86 kg m^{-2}. The most common deformation patterns formed in the perforated plate after the test are shown in Fig. 9a. The damage area spreads over three or more numbers of holes, typically three, as shown in the same figure. Macroscopically, the fracture seems brittle, while ductile bulge formation occurs at the back side of the perforated plate. After the four shots, the penetration depth on the base armor measured is 1.8 mm. There is no evidence of sharp intrusion in the base plate as shown in Fig. 9b and c. As the nose of bullet core was significantly eroded or the bullet core fractured into many pieces (Fig. 10), it did not cause sharp dents on the base plate. The inclination of the core and erosion at the tip of the nose can be seen in Fig. 10. At top right of Fig. 10, the picture of the original form of bullet core is shown to visualize how much erosion occurred after the core perforated the perforated plate. The inclination of the hardened steel core is about ~15°. The time frame of the bullet hitting the base armor plate could not be recorded due to the formation of a high flash in front of the core. It is not directly seen from the figure that the structural integrity of steel core retained during passing through perforated plate; at least front half of the projectile continued its travel toward the base plate. The projectile fracture into two pieces after the impact on the monolithic perforated plates was also shown previously [7,8,12].
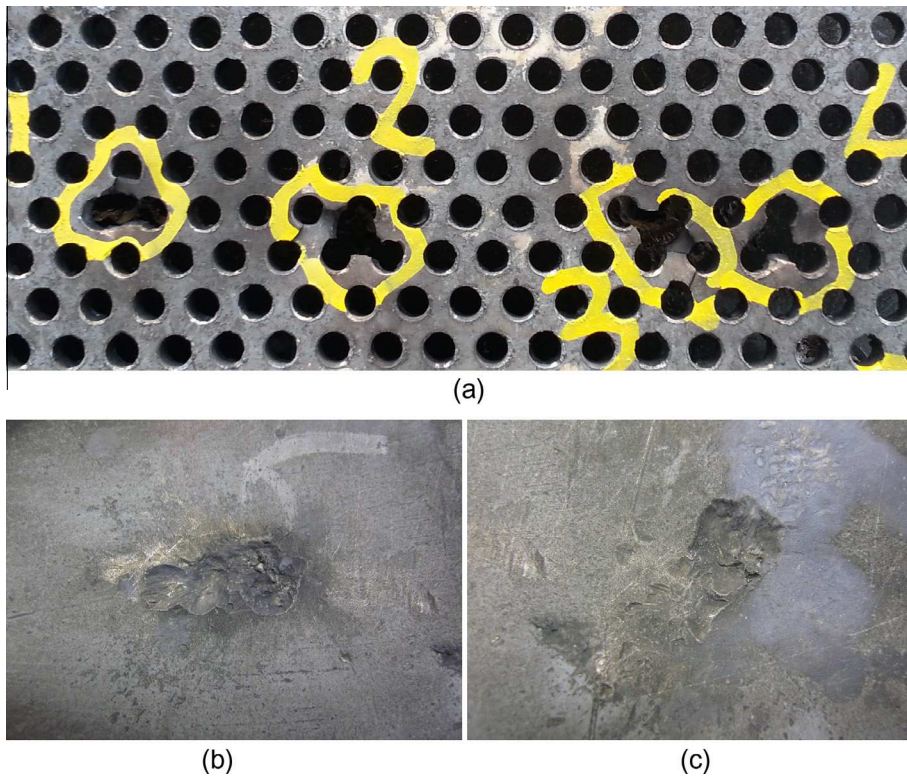

Fig. 9. (a) Layered armor plate front face (perforated plate) after the test, (b) base plate front face after the first shot and (c) base plate front face after the third shot.
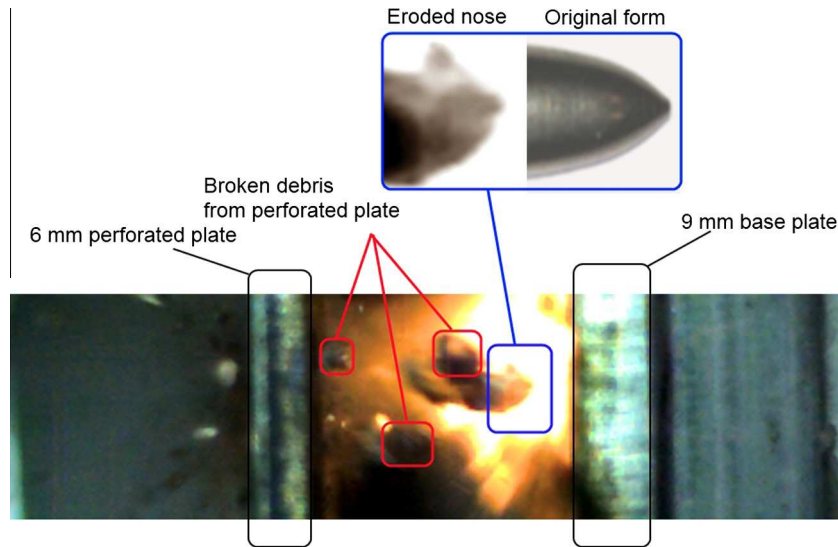
Fig. 10. High speed camera picture of the layered armor plates at $t = 0.07$ ms.

In all shots, the damage locations of the perforated and base plate did not coincide, indicating that yaw induction of the incoming bullet was achieved. The maximum inclination of the bullet was calculated 25°. The effect of obliquity of high hardness armor on shattering behavior of AP projectiles was previously investigated and shown both numerically and experimentally that the projectile broke into two pieces for the obliquities 20° and 30° and total shattering to the projectile occurred for obliquities higher than 45° [34]. Therefore, the calculated obliquity itself is not expected to result in shattering of the bullet and tip erosion may be considered as the secondary mechanism to explain total shattering evidences found on the base plate as shown in Fig. 9b and c. The dents formed on the base plate were previously taken as the indication of the bullet core fracture [7]. The three dents on the base plate seen in Fig. 9b and the shallow dents on base plate in Fig. 9c tend to conclude the shattering of the bullet. Two main defeating mechanisms were previously reported for the perforated plates [2,9]; the bullet inclination and the breakage of bullet due to bending effects.

Four different cases are investigated in the simulations of the ballistic testing of the perforated plate of the layered armor; the bullet hits (a) at the center of a hole (b) the side of a hole (c) at the middle of two holes and (d) at the geometric center of three holes. The simulations results for these four cases are sequentially shown in Fig. 11a–d at various times. In the first case shown in Fig. 11a, the bullet brass jacket is separated from bullet at about $t = 0.04$ ms without changing the incident angle ($t = 0.07$ and 0.1 ms). The bullet perforates the base armor and is captured while passing through the plate ($t = 0.10$ ms). This situation is considered as the failure since tip of the bullet has already passed the base armor. In the second case shown in Fig. 11b, the bullet hits the perforated plate at the side of a hole ($t = 0.04$ ms) and the projectile angle is significantly disturbed and deviates from its incident angle ($t = 0.06$ ms). The bullet steel core penetrates into the base armor at an elevated position ($t = 0.08$ ms). Penetration depth on the base armor is around 6 mm, indicating that the perforated plate assembly was captured the bullet successively. The defeating mechanism in this case is the changing incoming projectile angle as previously reported in Refs. [2,9]. In the third case shown in Fig. 11c, the bullet hits the perforated plate at the middle of two holes ($t = 0.04$ ms) and the bullet incident trajectory does not chance ($t = 0.06$ ms). Since the symmetry and the distance between the holes are greater than the bullet diameter, no side force acts on the bullet to deviate

from its incident trajectory. The base armor is perforated but captures the bullet before it completely passes through the plate ($t = 0.12$ ms). This situation is also a rare case, since the bullet hitting at the geometric center of two holes has a low probability. However, decreasing the distance between the holes will significantly reduce the probability of the occurrence of the third case. In the fourth case shown in Fig. 11d, the bullet hitting at the center of three holes, similar penetration behavior occurs with the third case. This is also an idealized case with low probability.

Although, the bending effect of the perforated plate on the bullet and the disturbance on the projectile trajectory are successfully modeled, the simulation penetration depths of the base armor (min 6 mm for the second case) are significantly higher than that of the ballistic test (1.8 mm). This shows that the deviating the projectile trajectory cannot be the only reason for the bullet defeat mechanism in the perforated plate. It was previously shown in the testing of the perforated plates that the bullet fracture initiated in the region between one third and two thirds of the length when bullet hit edge of a plate [9]. The von-Misses stress distributions of the steel core are shown at various times in Fig. 12 for the second case. As depicted in Fig. 12, the location of the maximum shear stress is close to the middle of the core, agreed with Ref. [9]. During penetration the bending stress as seen in Fig. 12 reaches a value of 2500 MPa, which can be taken as a threshold to initiate failure. Further modeling was implemented for the second case by applying a superficial failure criterion to the bullet to delete the elements when the tensile stress reached 2500 MPa. In this model, the jacket, sabot and fillers were excluded during post processing to identify merely the stress on the core. A similar approach was previously used to simulate the bullet shattering on the high hardness targets [34,35]. The simulation results are shown in Fig. 13 as function of time. As shown in Fig. 13, at the very beginning of the intrusion inside the perforated plate, around 0.015 ms, the equivalent von-Misses stress rises up to 1750 MPa, and reaches a critical value of 2500 MPa around 0.02 ms. The bullet core fractures at its middle point during the passage of perforated plate ($t = 0.02$ ms) and half of it penetrates into base armor ($t = 0.10$ ms). With the core fracture, the penetration depth on the base armor decreases; but still the numerical penetration depth is 3.5 mm higher than that of experiments. This tends to conclude that yaw formation combined with the breakage of the projectile into two pieces is not sufficient to simulate the deformation depth of the base target.
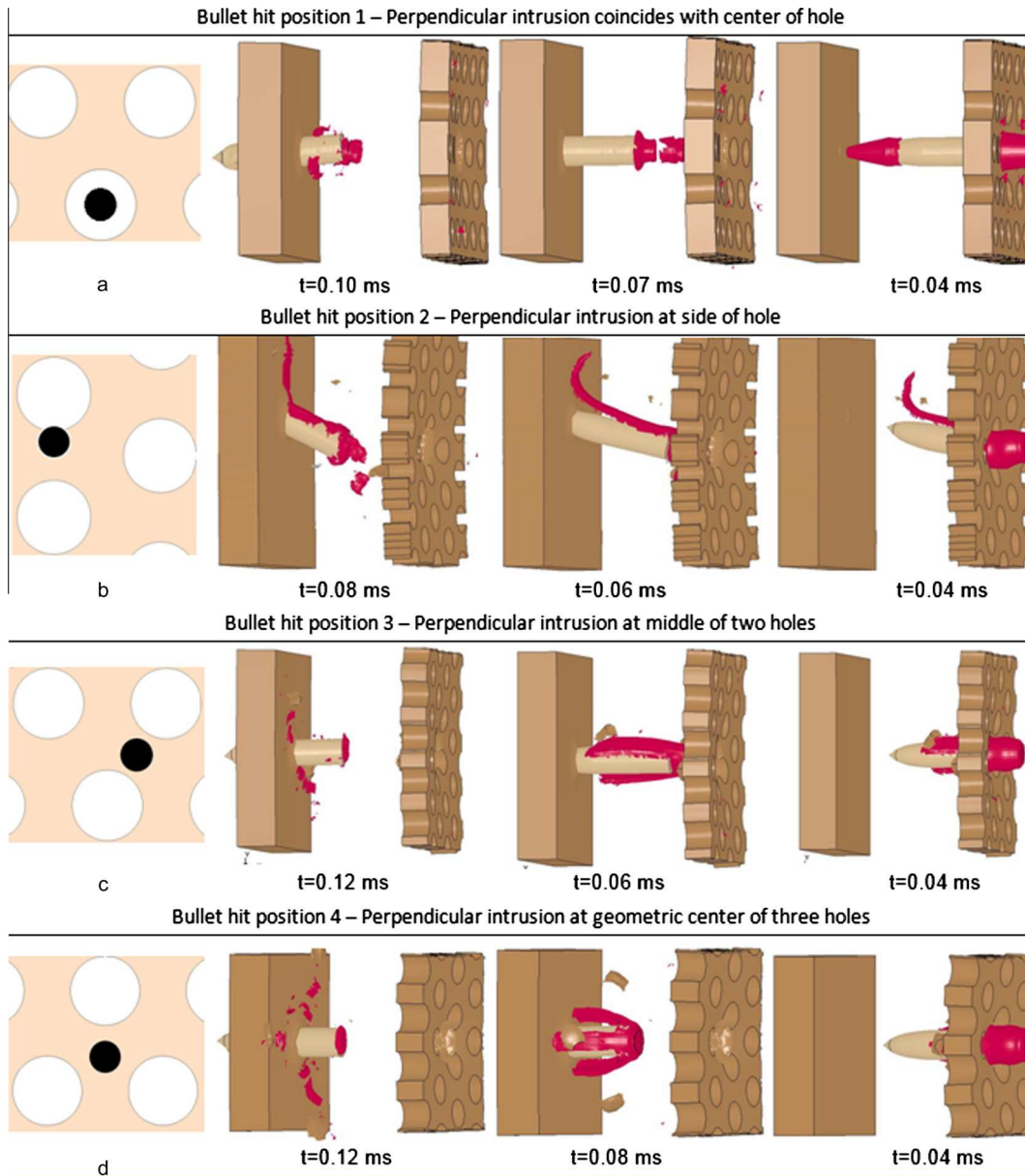
Bullet hit position 1 – Perpendicular intrusion coincides with center of hole

| a | t=0.10 ms | t=0.07 ms | t=0.04 ms |

Bullet hit position 2 – Perpendicular intrusion at side of hole

| b | t=0.08 ms | t=0.06 ms | t=0.04 ms |

Bullet hit position 3 – Perpendicular intrusion at middle of two holes

| c | t=0.12 ms | t=0.06 ms | t=0.04 ms |

Bullet hit position 4 – Perpendicular intrusion at geometric center of three holes

| d | t=0.12 ms | t=0.08 ms | t=0.04 ms |

Fig. 11. The sequences of bullet penetration through the perforated and base armor plate for the cases: the bullet hits (a) at the center of a hole (b) the side of a hole (c) at the middle of two holes and (d) at the geometric center of three holes.
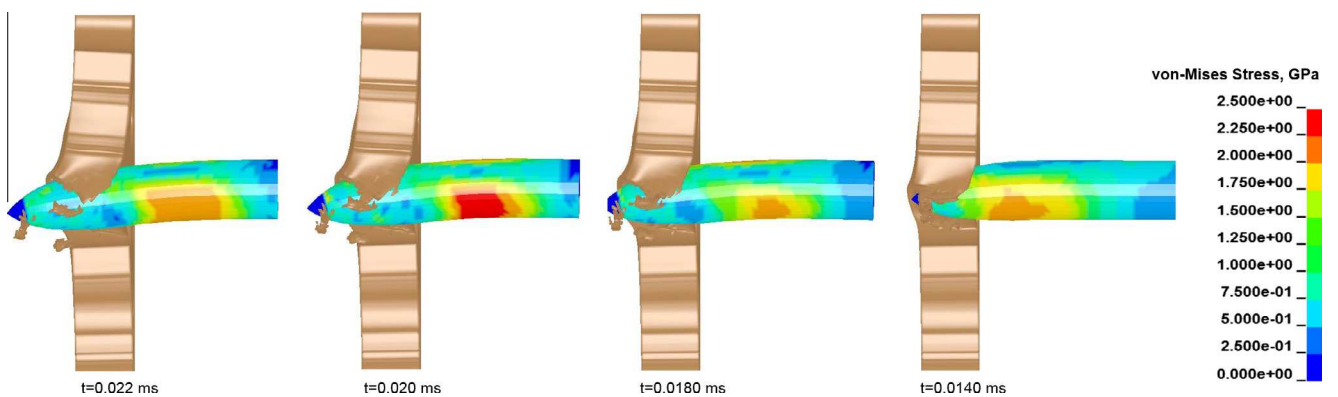

t=0.022 ms   t=0.020 ms   t=0.0180 ms   t=0.0140 ms

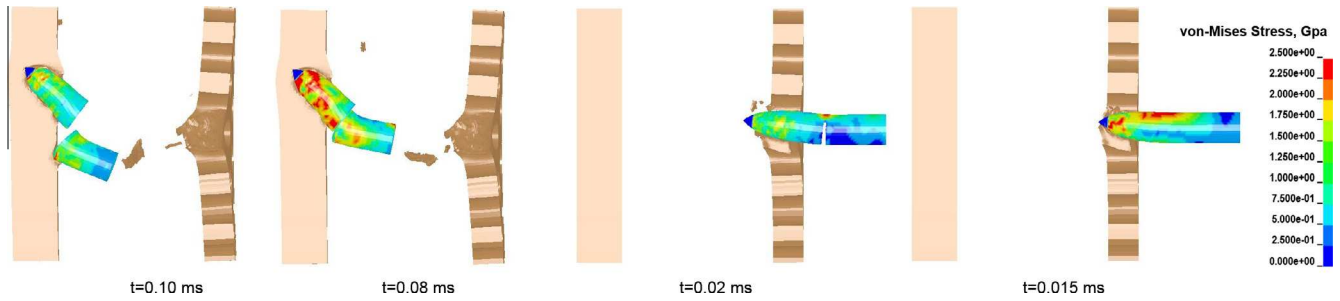**Fig. 12.** Maximum shear stress on the bullet core for the second case.

Fig. 13. Maximum equivalent stress on the bullet core projectile through the penetration of the perforated plate with von-Misses failure criteria for the second case.
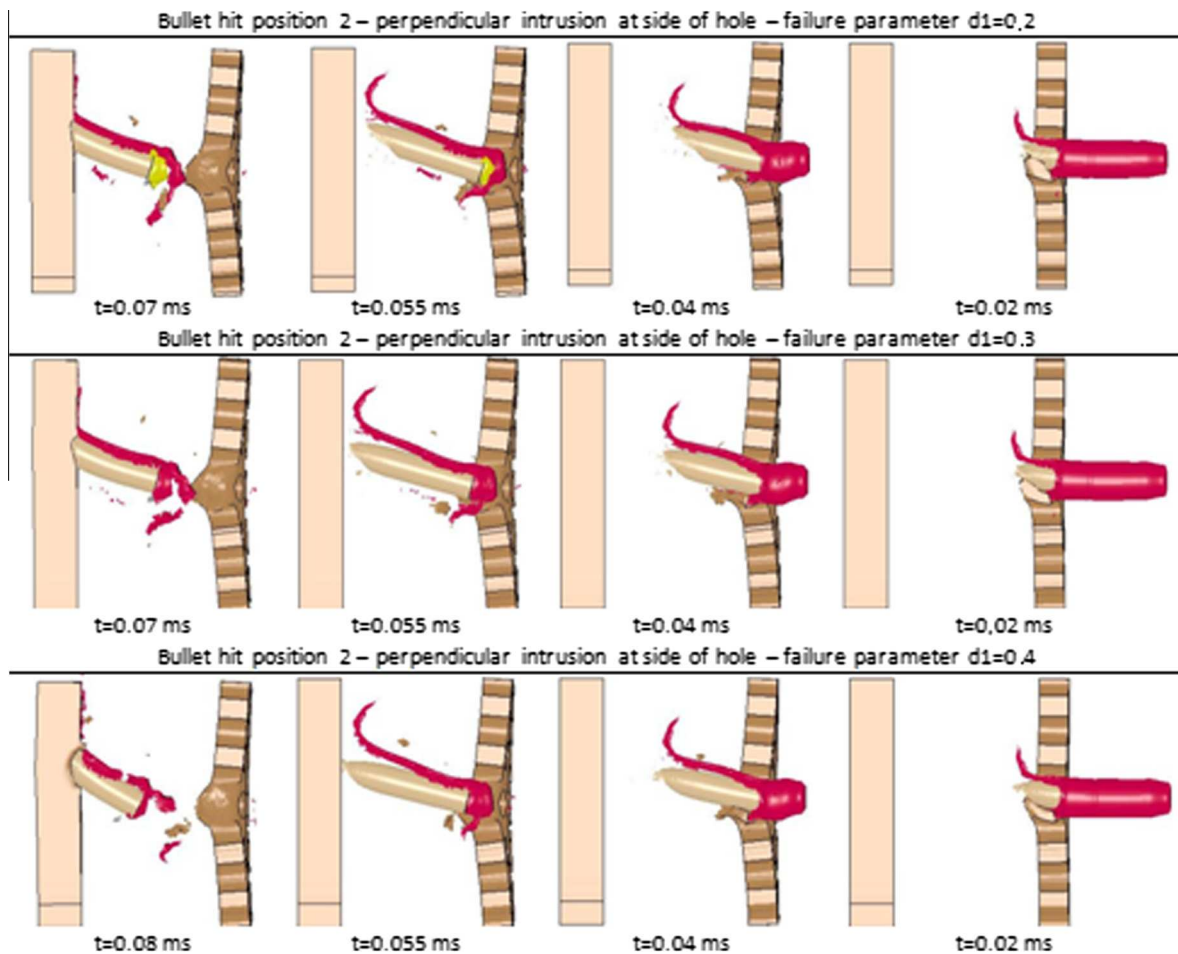

Fig. 14. Penetration sequences of the bullet with the *J–C* failure parameters for the second case.

In the monolithic plate, the main defeating mechanism to stop armor piercing projectile is the strain energy exerted to projectile by the armor. The deformation of the bullet tip has relatively less effect on the penetration depth. In order to determine whether bullet erosion can affect the penetration depth of the base armor plate, additional erosion criterion was introduced into model. In the tensile tests of the armor plate, the true strain reached a value of 16% at $600\,s^{-1}$ and up to 20% in the quasi-static tests [27]. Therefore, the erosion strain thresholds of 0.2, 0.3 and 0.4 were applied to the bullet nose. The simulation results are shown in Fig. 14 as function of time and erosion strain threshold. The perforated plate induces a bending force on the bullet and changes the incident angle of the bullet (*t* = 0.04 ms). Meanwhile, the tip of the projectile erodes, the erosion being highest when the erosion strain threshold is 0.2. The erosion significantly reduces the penetration capability of the bullet as seen in Fig. 14. The numerical penetration depth is measured 1.4 mm when the erosion strain threshold is 0.4, which is comparable with the experimental penetration depth, 1.8 mm. The simulation and experimental front face damages on the perforated plate are shown in Fig. 15(a–d) using core failure model and erosion strain threshold of 0.4. The simulation and experimental damage patterns are seen to be very similar on the perforated plate. Edge effects are clearly seen both in the simulations and experiments.
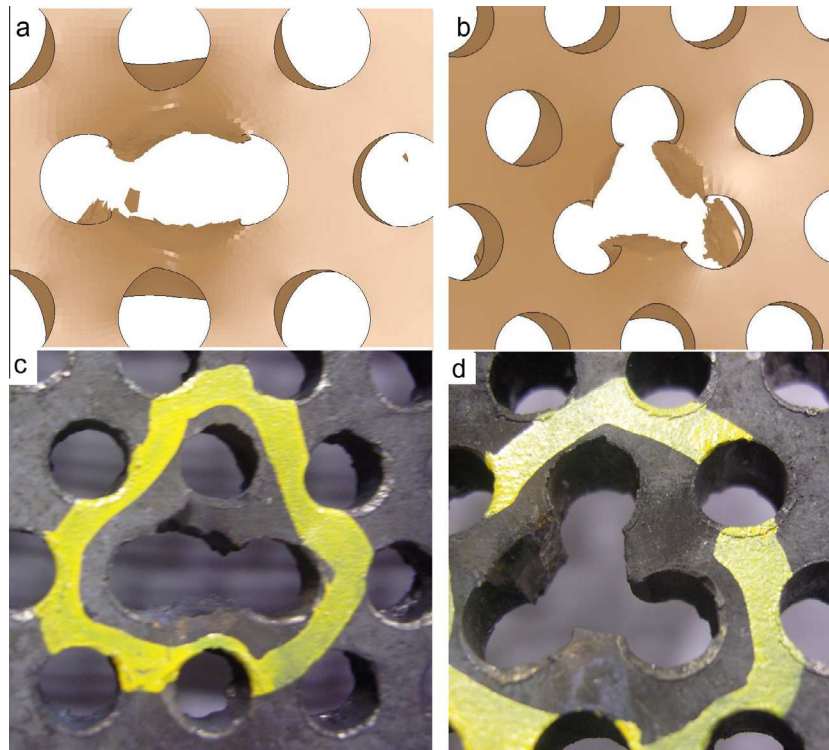
Fig. 15. (a) and (b) The simulation and (c) and (d) experimental front face damages on the perforated plate after the ballistic tests.

5. Conclusions

The bullet defeating mechanisms of a high hardness steel layered armor (composed of monolithic base armor and perforated add-on armor) was investigated both experimentally and numerically. The numerical models were developed using Lagrange discretization in Ls-Dyna with various cases including without and with bullet failure model. The fidelity of the model material parameters were verified through ballistic testing and modeling of the monolithic plates in two different thicknesses. The defeating mechanisms of the bullet in testing layered armor were proved through experiments and simulations to include (a) asymmetric forces causing the projectile to deviate from incident trajectory, (b) the bullet core fracture and (c) the bullet core nose erosion. With these mechanisms, well agreements were shown between the simulation and experimental penetration depths of the base armor and the deformation patterns of the perforated plate after the ballistic tests. The results also implied that high hardness multilayer perforated plates could be used effectively in ballistic protection and had a potential of decreasing areal mass efficiency significantly.

References

[1] Haque BZ, Kearney MM, Gillespie Jr JW. Advances in protective personnel and vehicle armors. Recent Pat Mater Sci 2012;5:103–34.
[2] Ben-Moshe D. Patent No.: EP 0 209 221 A1. An armor assembly for armored vehicles; 1986.
[3] Auyer RA, Buccellato RJ, Gidynski AJ, Ingersol RM, Sridharan S. Patent No.: 5,014,593. Perforated plate armor; 1991.
[4] Ravid M, Hirchberg Y. Patent No.: 7,513,186 B2. Ballistic armor; 2009.
[5] Norris WJ, Smith CA. Patent No.: WO 21010/036411 A2. Perforated armor with geometry modified for lighter weight; 2010.
[6] Madhu V, Bhat TB. Armour protection and affordable protection for futuristic combat vehicles. Defence Sci J 2011;61:394–402.
[7] Balos S, Grabulov V, Sidjanin L, Pantic M, Radisavljevic I. Geometry mechanical properties and mounting of perforated plates for ballistic application. Mater Des 2009;31:2916–24.
[8] Radisavljevic I, Balos S, Nikacevic M, Sidjanin L. Optimization of geometrical characteristics of perforated plates. Mater Des 2013;49:81–9.
[9] Mishra B, Jena PK, Ramankrishna B, Mahdu V, Bhat TB, Gupta NK. Effect of tempering temperature, plate thickness and presence of holes on ballistic impact behavior and ASB formation of a high strength steel. Int J Impact Eng 2012;44:17–28.
[10] Mishra B, Ramankrishna B, Jena PK, Kumar SV, Mahdu V, Gupta NK. Experimental studies on the effect of size and shape of holes on damage and microstructure of high hardness armour steel plates under ballistic impact. Mater Des 2013;43:17–24.
[11] Howel R, Montgomery JS, Van Aken DC. Advancements in steel for weight reduction of P900 armor plate. In: Proceedings of 26th army science conference Orlando; 2008.
[12] Chocron S, Anderson CE, Grosch D, Popelar CH. Impact of the 7.62 mm APM2 projectile against the edge of a metallic target. Int J Impact Eng 2001;25:423–37.
[13] Rosenberg Z, Ashuach Y, Yeshurun Y, Dekel E. On the main mechanism for defeating AP projectiles, long rods and shaped charge jets. Int J Impact Eng 2009;36:588–96.
[14] Abaqus Theory Manual. Version 6.7; 2007.
[15] MSC.DYTRAN Theory Manual Version 2005. MSC. Software Corporation.
[16] Sph User Manual & Tutorial, Revision 4.3; 2005. Century Dynamics Inc.
[17] LS-Dyna Keyword User's Manual Version 971, 2007. Livermore Software Technology Corporation (LSTC).
[18] Borvik T, Langseth M, Hopperstad OS, Malo KA. Ballistic penetration of steel plates. Int J Impact Eng 1999;22:855–86.
[19] Buchar J, Voldrich J, Rolc S, Lisy J. Ballistic performance of dual hardness armor. In: Proceedings of 20th international symposium on ballistics, Orlando; 2002, p. 23–27.
[20] Borvik T, Hopperstad OS, Berstad T, Langeseth M. Perforation of 12 mm thick steel plates by 20 mm diameter projectiles with flat, hemispherical and conical noses Part II: numerical simulations. Int J Impact Eng 2002;27:37–64.
[21] Teng X, Wierzbicki T, Huang M. Ballistic resistance of double-layered armor plates. Int J Impact Eng 2008;35:870–84.
[22] Dey S, Borvik T, Teng X, Wierzbicki T, Hopperstad OS. On the ballistic resistance of double-layered steel plates: an experimental and numerical investigation. Int J Solids Struct 2007;44:6701–23.
[23] Borvik T, Dey S, Clausen AH. Perforation resistance of five different high-strength steel plates subjected to small arms projectiles. Int J Impact Eng 2009;36:948–64.
[24] NATO STANAG 4569. Protection levels for occupants of logistic and light armored vehicles, 1st ed.; 2004.
[25] Johnson GR, Cook WH. A constitutive model and data for metals subjected to large strains, high strain rates and high temperatures. In: Proceedings of the 7th international symposium on ballistics, Hauge, Netherlands; 1983, p. 541–547.

[26] Johnson GR, Cook WH. Fracture characteristics of three metals subjected to various strains, strain rates, temperatures and pressures. Eng Fract Mech 1985;21:34–48.

[27] Kilic N, Ekici B. Ballistic resistance of high hardness armor steels against 7.62 mm armor piercing ammunition. Mater Des 2013;44:35–48.

[28] Cakircali M, Kilicaslan C, Guden M, Kiranli E, Shchukin VY, Petronko VV. Cross wedge rolling of a Ti6Al4V (ELI) alloy: the experimental studies and the finite element simulation of the deformation and failure. Int J Adv Manuf Technol 2013;65:1273–87.

[29] Skoglund P, Nilsson M, Tjernberg A. Fracture modeling of a high performance armor steel. J Phys IV France 2006;134:197–202.

[30] Nilsson M. Constitutive model for Armox 500T and Armox 600T at low and medium strain rates. FOI, Swedish Defence Research Agency, TR FOI-R-1068-SE; 2003.

[31] Nsiampa N, Coghe F, Dykmans G. Numerical investigation of the bodywork effect. DYMAT 2009:1561–6.

[32] Niezgoda T, Morka A. On the numerical methods and physics of perforation in the high-velocity impact mechanics. World J Eng 2010:414–7.

[33] Zukas JA. Introduction to hydrocodes. Elsevier; 2004.

[34] Rosenberg Z, Dekel E. Terminal ballistics. Springer; 2012.

[35] Danesjou K, Shahravi M. The role of simulation in long rod ricochet phenomenon. Mech Aerospace Eng J 2008;3:69–86.

[36] Preece DS, Berg VS. Bullet impact on steel and Kevlar/steel armor – computer modeling and experimental data. In: ASME Symposium on structures under extreme loading, San Diego; 2004.